

# Temperature-Induced Magnonic Chern Insulator in Collinear Antiferromagnets

Yun-Mei Li,<sup>1,\*</sup> Xi-Wang Luo,<sup>2</sup> and Kai Chang<sup>3</sup>

<sup>1</sup>*Department of Physics, School of Physical Science and Technology, Xiamen University, Xiamen 361005, China*

<sup>2</sup>*CAS Key Laboratory of Quantum Information, University of Science and Technology of China, Hefei 230026, China*

<sup>3</sup>*SKLSM, Institute of Semiconductors, Chinese Academy of Sciences, P.O. Box 912, Beijing 100083, China*

Thermal fluctuation in magnets will bring temperature-dependent self-energy corrections to the magnons, however, their effects on the topological orders of magnons is not well explored. Here we demonstrate that such corrections can induce a Chern insulating phase in two-dimensional collinear antiferromagnets with sublattice asymmetries by increasing temperature. We present the phase diagram of the system and show that the trivial magnon bands at zero temperature exhibit Chern insulating phase above a critical temperature before the paramagnetic phase transition. The self-energy corrections close and reopen the bandgap at  $\Gamma$  or  $\mathbf{K}$  points, accompanied by a magnon chirality switch and nontrivial Berry curvature transition. The thermal Hall effect of magnons or detecting the magnon polarization can give experimentally prominent signatures of topological transitions. We include the numerical results based on van der Waals magnet MnPS<sub>3</sub>, calling for experimental implementation. Our work presents a new paradigm for constructing topological phase that is beyond the linear spin wave theory.

## I. INTRODUCTION

The last twenty years have witnessed the extraordinary developments of topological insulators and semimetals in the field of condensed matter physics.<sup>1–14</sup> In analog to electronic systems, the topological phases have also been extended to the bosonic systems, such as the photonic<sup>15</sup> and acoustic systems.<sup>16</sup> Magnons, quantized spin excitations in magnets, another boson, are also proposed to host nontrivial topological phases, realized in magnets with artificially designed structures,<sup>17–19</sup> special crystal symmetries,<sup>20–28</sup> or the quantum fluctuations.<sup>29</sup> The emergence of edge or surface states immune to disorder and back scattering has great potential applications for designing magnonic devices<sup>30,31</sup> with low dissipation and power consumption.

One of the key features in magnetic systems is the presence of magnon-magnon interactions (MMIs) and thermal fluctuation. Their interplay would give rise to temperature-dependent nonlinear self-energy corrections to the magnons.<sup>32–39</sup> Recent two works<sup>28,29</sup> stated that the nonlinear corrections can drive a topological phase transition of Dirac magnons hosting opposite Chern numbers at a critical temperature. The other works discussed the magnon topology within the linear spin wave theory<sup>17–27,44</sup> or only the magnon renormalization effect.<sup>35–39</sup> None of them addressed the possibilities of realizing topological phases of magnons above a finite temperature  $T_c$  while the bands below  $T_c$  are topologically trivial with  $T_c$  below the Curie or Néel temperature. This is quite reasonable because the specific schemes responsible for the topological phases at zero temperature are always present or absent in the self-energies at finite temperature. This picture explains why few works made explorations on the construction of a topological phase at finite temperature.

In this paper, we show that increasing temperature can actually induce topological phase for magnons by considering the two-dimensional collinear antiferromagnet MnPS<sub>3</sub> as the example. We introduce sublattice asym-

metric magnetic interactions induced in heterostructures, breaking the  $\mathcal{PT}$  symmetry and magnon band degeneracy. We find that at zero temperature, the Chern insulating phase emerges, but only exists in a finite interval of the single-ion easy-axis anisotropy strength. The self-energy corrections do not destroy this topological phase. Outside the interval, the magnon bands are topologically trivial at  $T = 0$ . But as temperature increases, due to the self-energies, the bandgap at  $\Gamma$  or  $\mathbf{K}$  points will be closed and reopen above a critical temperature  $T_c$ , which is well below the Néel temperature. The topological invariant, i.e., the Chern integer of the acoustic branch changes from 0 to 1 across  $T_c$ . We also find that the bandgap closing and reopening are accompanied by a magnon chirality switch and nontrivial Berry curvature transition near  $\Gamma$  or  $\mathbf{K}$  points. The thermal Hall effect gives prominent signatures for the topological phase transitions near  $\Gamma$  point. Also detecting the magnon polarization provides another experimental proofs. Our proposal and conclusion are quite universal in collinear antiferromagnets, and can be extended to ferrimagnets.

This paper is organized as follows. In Sec. II, we present the model and use the finite-temperature field theory to deal with the MMIs. In Sec III, we calculate the magnon bands at both zero and finite temperatures and the corresponding topological invariant. We present the phase diagram and discuss topological phase induced by increasing the temperature. We also give the thermal Hall effect and magnon chirality switch during the topological phase transitions, which can be probed in realistic experiments. Finally, we summarize in Sec. IV.

## II. MODEL AND METHODOLOGY

We consider a honeycomb collinear antiferromagnet, as illustrated in Fig. 1. the spin interaction Hamiltonian is

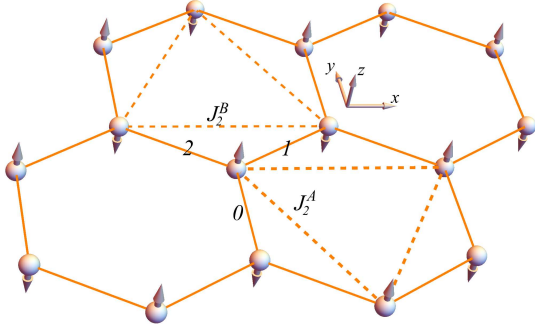


FIG. 1: Illustration of the honeycomb antiferromagnet with sublattice asymmetry. The numbers denote the bond index. Spins on A-sublattice point up while on B-sublattice point down. The intra-sublattice second neighbor interactions on two sublattices are denoted as  $J_2^A$  and  $J_2^B$ , respectively.

given by

$$H = J_1 \sum_{\langle ij \rangle} \mathbf{S}_i \cdot \mathbf{S}_j + I_1 \sum_{\langle ij \rangle} S_i^z S_j^z + \sum_{\langle\langle ij \rangle\rangle} J_2^{ij} \mathbf{S}_i \cdot \mathbf{S}_j + \frac{J_a}{2} \sum_{\langle ij \rangle} (\gamma_{ij} S_i^+ S_j^+ + \gamma_{ij}^* S_i^- S_j^-) - \sum_i K_i (S_i^z)^2. \quad (1)$$

The first and second term denote the Heisenberg exchange interactions between nearest neighbor with an Ising-type exchange anisotropy characterized by  $I_1$ . The third term denotes the Heisenberg exchange interactions between second neighbors, describing the interactions between spins in the same A or B sublattices (Fig. 1), characterized by  $J_2^A$  and  $J_2^B$ , respectively. Here we assume  $J_2^A \neq J_2^B$ . The fourth term is the bond-dependent interactions<sup>40</sup> between nearest neighbor, allowed by the symmetry and consistent with recent experiment in MnPS<sub>3</sub>.<sup>41</sup>  $\gamma_{ij} = e^{i2\pi n/3}$  with  $n = 0, 1, 2$  the bond index, as illustrated in Fig. 1. The last term is the sublattice asymmetric single-ion easy-axis anisotropy, characterized by  $K_A$  and  $K_B$  for the two sublattices, respectively. The Hamiltonian above with  $J_2^A = J_2^B$  and without  $K_A, K_B$  was proposed for MnPS<sub>3</sub>.<sup>40</sup> The exchange anisotropy  $I_1$ , difference between  $J_2^A$  and  $J_2^B$ , and anisotropy field  $K_A, K_B$  can be induced or tuned in the MnPS<sub>3</sub> homobilayer or in MnPS<sub>3</sub>/CrCl<sub>3</sub> heterostructure, verified in the very recent first-principles calculations.<sup>42,43</sup> For negative and quite small positive  $J_2^A$  and  $J_2^B$ , the ground state stays in collinear AFM phase.<sup>45,46</sup>

We apply the Holstein-Primakoff transformation,  $S^z = S - a^\dagger a$ ,  $S^+ = \sqrt{2S} - a^\dagger a a$ ,  $S^- = a^\dagger \sqrt{2S} - a^\dagger a$  for A-sublattice, and  $S^z = -S + b^\dagger b$ ,  $S^+ = b^\dagger \sqrt{2S} - b^\dagger b$ ,  $S^- = \sqrt{2S} - b^\dagger b b$  for B-sublattice. The Hamiltonian in Eq. (1) can be expanded as  $H = \sum_{p=0}^{\infty} H_{2p}$ , where  $2p$  denote the number of bosonic operators. We here keep the terms up to quartic order and neglect the ground state energy term. With a Fourier transformation, the two-particle term can be written in the form  $H_2 = \frac{1}{2} \sum_{\mathbf{k}} \Psi_{\mathbf{k}}^\dagger H_{\mathbf{k}} \Psi_{\mathbf{k}}$ , where  $\Psi_{\mathbf{k}} = (a_{\mathbf{k}}, b_{\mathbf{k}}, a_{-\mathbf{k}}^\dagger, b_{-\mathbf{k}}^\dagger)^T$ , the uppercase denote

the transpose. We have

$$H_{\mathbf{k}} = \begin{pmatrix} h_{\mathbf{k}} & \Delta_{\mathbf{k}} \\ \Delta_{\mathbf{k}}^\dagger & h_{-\mathbf{k}}^T \end{pmatrix}, \quad (2)$$

where  $h_{\mathbf{k}} = h_0 \mathbb{I}_2 + \mathbf{h} \cdot \boldsymbol{\sigma}$ ,  $\Delta_{\mathbf{k}} = \boldsymbol{\delta} \cdot \boldsymbol{\sigma}$ .  $\boldsymbol{\sigma}$  denotes the sublattice index, with  $h_0 = (h_A + h_B)/2$ ,  $h_x = J_a S \text{Re}(g_{\mathbf{k}})$ ,  $h_y = -J_a S \text{Im}(g_{\mathbf{k}})$ ,  $h_z = (h_A - h_B)/2$ ,  $\delta_x = J_1 S \text{Re}(f_{\mathbf{k}})$ ,  $\delta_y = -J_1 S \text{Im}(f_{\mathbf{k}})$ ,  $h_A = K_A(2S - 1) + 3(J_1 + I_1)S - J_2^A S(6 - d_{\mathbf{k}})$ ,  $h_B = K_B(2S - 1) + 3(J_1 + I_1)S - J_2^B S(6 - d_{\mathbf{k}})$ ,  $g_{\mathbf{k}} = 1 + 2e^{i\frac{3}{2}k_y} \cos(\frac{\sqrt{3}}{2}k_x + \frac{2\pi}{3})$ ,  $f_{\mathbf{k}} = 1 + 2e^{i\frac{3}{2}k_y} \cos(\frac{\sqrt{3}}{2}k_x)$ ,  $d_{\mathbf{k}} = \sum_{i=1}^6 \cos(\mathbf{k} \cdot \mathbf{a}_i)$ ,  $\mathbf{a}_i$  is the second neighbor lattice vectors.

We now discuss the effect of MMIs, i.e. the four-particle term  $H_4$ . We have

$$H_4 = -\frac{1}{N} \sum_{\{\mathbf{k}_i\}} \frac{J_1}{4} (f_{\mathbf{k}_4} a_{\mathbf{k}_1}^\dagger a_{\mathbf{k}_2} a_{\mathbf{k}_3} b_{\mathbf{k}_4} + f_{\mathbf{k}_4}^* b_{\mathbf{k}_1}^\dagger b_{\mathbf{k}_2} b_{\mathbf{k}_3} a_{\mathbf{k}_4} + H.c.) \delta_{\{\mathbf{k}_i\}} + [(J_1 + I_1) f_{\mathbf{k}_4 - \mathbf{k}_2} a_{\mathbf{k}_1}^\dagger b_{\mathbf{k}_2}^\dagger a_{\mathbf{k}_3} b_{\mathbf{k}_4} + \frac{J_a}{4} (g_{\mathbf{k}_3} a_{\mathbf{k}_1}^\dagger a_{\mathbf{k}_2}^\dagger b_{\mathbf{k}_3} a_{\mathbf{k}_4} + g_{\mathbf{k}_1} a_{\mathbf{k}_1}^\dagger b_{\mathbf{k}_2}^\dagger b_{\mathbf{k}_3} b_{\mathbf{k}_4} + H.c.) + (\epsilon_A a_{\mathbf{k}_1}^\dagger a_{\mathbf{k}_2}^\dagger a_{\mathbf{k}_3} a_{\mathbf{k}_4} + \epsilon_B b_{\mathbf{k}_1}^\dagger b_{\mathbf{k}_2}^\dagger b_{\mathbf{k}_3} b_{\mathbf{k}_4})] \delta_{\{\mathbf{k}_i\}}^2, \quad (3)$$

where  $\delta_{\{\mathbf{k}_i\}}^1 = \delta_{\mathbf{k}_1, \mathbf{k}_2 + \mathbf{k}_3 + \mathbf{k}_4}$ ,  $\delta_{\{\mathbf{k}_i\}}^2 = \delta_{\mathbf{k}_1 + \mathbf{k}_2, \mathbf{k}_3 + \mathbf{k}_4}$ ,  $\epsilon_{A,B} = J_2^{A,B} d_{\{\mathbf{k}_i\}} + K_{A,B}$  and  $d_{\{\mathbf{k}_i\}} = \frac{d_{\mathbf{k}_1} + d_{\mathbf{k}_4} - 2d_{\mathbf{k}_4 - \mathbf{k}_2}}{4}$ . To take the many-body effect and its interplay with thermal fluctuation into account, we employ the Green function method and define a matrix Green function as  $\hat{G}(\mathbf{k}, \tau) = -\langle T_\tau \Psi_{\mathbf{k}}(\tau) \Psi_{\mathbf{k}}^\dagger(0) \rangle$ ,<sup>47</sup> where  $T_\tau$  is the chronological operator for the imaginary time  $\tau$ . The Heisenberg operator is defined as  $A(\tau) = e^{\tau H} A(0) e^{-\tau H}$  and  $H = H_2 + H_4$  is Hermitian. The bracket denotes the thermal average. To get the solution, we solve the Heisenberg equation-of-motion for the Green function elements and apply the random phase approximation to extract the nonlinear self-energy corrections from MMIs. After a Fourier transformation  $\hat{G}(\mathbf{k}, \tau) = (1/\beta) \sum_n \hat{G}(\mathbf{k}, \omega_n) e^{-i\omega_n \tau}$  with  $\beta = 1/T$ , where  $T$  is the temperature and  $\omega_n$  is the bosonic Matsubara frequency, we can get the Dyson's equation  $\hat{G}^{-1}(\mathbf{k}, \omega_n) = i\omega_n \tau_z - H_{\mathbf{k}}^{\text{eff}}$  and the effective Hamiltonian

$$H_{\mathbf{k}}^{\text{eff}} = H_{\mathbf{k}} + \Sigma_{\mathbf{k}} = \begin{pmatrix} h_{\mathbf{k}}^{\text{eff}} & \Delta_{\mathbf{k}}^{\text{eff}} \\ (\Delta_{\mathbf{k}}^{\text{eff}})^\dagger & (h_{-\mathbf{k}}^{\text{eff}})^T \end{pmatrix}, \quad (4)$$

with  $h_{\mathbf{k}}^{\text{eff}} = h_0^{\text{eff}} \mathbb{I}_2 + \mathbf{h}^{\text{eff}} \cdot \boldsymbol{\sigma}$ .  $h_0^{\text{eff}} = (h_A^{\text{eff}} + h_B^{\text{eff}})/2$ ,  $h_x^{\text{eff}} = J_a \frac{(\bar{S}_A + \bar{S}_B)}{2} \text{Re}(g_{\mathbf{k}})$ ,  $h_y^{\text{eff}} = -J_a \frac{(\bar{S}_A + \bar{S}_B)}{2} \text{Im}(g_{\mathbf{k}})$ ,  $h_z = (h_A^{\text{eff}} - h_B^{\text{eff}})/2$ , where  $h_A^{\text{eff}} = K_A(-2S - 1 + 4\bar{S}_A) + 3(J_1 + I_1)\bar{S}_B - J_2^A \bar{S}_A(6 - d_{\mathbf{k}}) - h_A^r$ ,  $h_B^{\text{eff}} = K_B(-2S - 1 + 4\bar{S}_B) + 3(J_1 + I_1)\bar{S}_A - J_2^B \bar{S}_B(6 - d_{\mathbf{k}}) - h_B^r$ ,  $\bar{S}_A = S - \frac{1}{N} \sum_{\mathbf{q}} \langle a_{\mathbf{q}}^\dagger a_{\mathbf{q}} \rangle$ ,  $\bar{S}_B = S - \frac{1}{N} \sum_{\mathbf{q}} \langle b_{\mathbf{q}}^\dagger b_{\mathbf{q}} \rangle$ ,  $\bar{S}_A^r = S + \frac{1}{6N} \sum_{\mathbf{q}} d_{\mathbf{q}} \langle a_{\mathbf{q}}^\dagger a_{\mathbf{q}} \rangle - \frac{1}{N} \sum_{\mathbf{q}} \langle a_{\mathbf{q}}^\dagger a_{\mathbf{q}} \rangle$ ,  $\bar{S}_B^r = S + \frac{1}{6N} \sum_{\mathbf{q}} d_{\mathbf{q}} \langle b_{\mathbf{q}}^\dagger b_{\mathbf{q}} \rangle - \frac{1}{N} \sum_{\mathbf{q}} \langle b_{\mathbf{q}}^\dagger b_{\mathbf{q}} \rangle$ ,  $h_A^r = h_B^r = \frac{J_1}{N} \text{Re} \sum_{\mathbf{q}} f_{\mathbf{q}} \langle a_{\mathbf{q}}^\dagger b_{-\mathbf{q}}^\dagger \rangle + \frac{J_a}{N} \text{Re} \sum_{\mathbf{q}} g_{\mathbf{q}} \langle a_{\mathbf{q}}^\dagger b_{\mathbf{q}} \rangle$ ,  $(\Delta_{\mathbf{k}}^{\text{eff}})_{12} = \frac{(\bar{S}_A + \bar{S}_B)}{2} J_1 f_{\mathbf{k}} - (J_1 + I_1) \sum_{\mathbf{q}} f_{\mathbf{k} - \mathbf{q}} \langle a_{\mathbf{q}} b_{-\mathbf{q}} \rangle$ ,

$(\Delta_{\mathbf{k}}^{\text{eff}})_{21} = (\Delta_{-\mathbf{k}}^{\text{eff}})_{12}$ . The other terms during the random phase approximation always vanish, are thus neglected. By diagonalizing the effective Hamiltonian in Eq. (4),  $\Lambda_{\mathbf{k}}^\dagger H_{\mathbf{k}}^{\text{eff}} \Lambda_{\mathbf{k}} = \text{diag}\{E_{\mathbf{k}}, E_{-\mathbf{k}}\}$ , we have  $H_{\mathbf{k}}^{\text{eff}} = \sum_{\mathbf{k}} (E_{\mathbf{k}}^\alpha \alpha_{\mathbf{k}}^\dagger \alpha_{\mathbf{k}} + E_{\mathbf{k}}^\beta \beta_{\mathbf{k}}^\dagger \beta_{\mathbf{k}})$  up to zero-point energy. The paraunitary eigenvectors satisfy  $\Lambda_{\mathbf{k}}^\dagger \tau_z \Lambda_{\mathbf{k}} = \tau_z$  and  $\tau_z$  is the Pauli matrix acting on the particle-hole space.<sup>17</sup> Note that the diagonalization gives us the relation  $\Psi_{\mathbf{k}} = \Lambda_{\mathbf{k}} \Phi_{\mathbf{k}}$  with  $\Phi_{\mathbf{k}} = (\alpha_{\mathbf{k}}, \beta_{\mathbf{k}}, \alpha_{-\mathbf{k}}^\dagger, \beta_{-\mathbf{k}}^\dagger)^T$ .

The additional terms in Eq. (4) compared to Eq. (2) is the self-energy term  $\Sigma_{\mathbf{k}}$ . Using the relation  $\Psi_{\mathbf{k}} = \Lambda_{\mathbf{k}} \Phi_{\mathbf{k}}$ , the matrix element of self-energy can be expressed as

$$\Sigma_{\mathbf{k}}^{ij} = \frac{1}{N} \sum_{\mathbf{q}, \lambda=\alpha, \beta} [T_{ij}^\lambda(\mathbf{k}, \mathbf{q}) n_{\mathbf{q}, \lambda}(T) + Q_{ij}^\lambda(\mathbf{k}, \mathbf{q})], \quad (5)$$

where  $n_{\mathbf{q}, \lambda}$  is the Bose-Einstein distribution function  $n_{\mathbf{q}, \lambda} = (e^{E_{\mathbf{q}}^\lambda/T} - 1)^{-1}$  with a zero chemical potential. The right two terms in Eq. (5) correspond to the thermal and quantum corrections, respectively. The calculation method of them are presented in Appendix A. Notice that the self-energy correction does not vanish even at zero temperature due to the quantum fluctuations. Similar to the previous work,<sup>38,39</sup> the Eqs. (4), (5) and diagonalization relation above form the self-consistent relations. We can calculate the band structures at given temperature self-consistently and obtain corresponding Chern integers. The results on temperature induced topological phases are presented below.

### III. RESULTS AND DISCUSSIONS

#### A. Phase diagram and topological transitions

We first discuss the topological phases at zero temperature  $T = 0$  to get an intuitive picture of the system. The two magnon bands are usually degenerate in pristine antiferromagnets. The sublattice asymmetric second neighbor exchange interaction and sublattice asymmetric single-ion easy-axis anisotropy break the band degeneracy. Especially, for  $J_2^A \neq J_2^B$ , the two magnon bands have different group velocities at the same energies even when  $K_A = K_B$ . That is to say, the two magnon bands will separate totally or show degeneracy at limited momenta. We find when  $J_a = 0$  and  $J_2^A > J_2^B$ , in the region  $0 < K_A - K_B < K_c$ , the two magnon bands will show a ring-like band intersection, as shown in Fig. 2 (a) by the solid lines. Here  $K_c \simeq 9(J_2^A - J_2^B)\bar{S}'/(4\bar{S} - 2S - 1)$  with  $\bar{S} = \bar{S}_A = \bar{S}_B$  and  $\bar{S}' = \bar{S}'_A = \bar{S}'_B$  at zero temperature. Here we have considered the quantum corrections. While at  $K_A = K_B$  ( $K_A = K_B + K_c$ ), the two bands show point touching at  $\Gamma$  ( $\mathbf{K}$  and  $\mathbf{K}'$ ) point(s) in the Brillouin zone (BZ). Outside the above interval, the two bands are always separated and topologically trivial even for  $J_a \neq 0$ .

Finite  $J_a$  is expected to gap the two bands and bring a nontrivial topology when  $0 < K_A - K_B < K_c$ . As  $\mathbf{g}_{\mathbf{k}}$

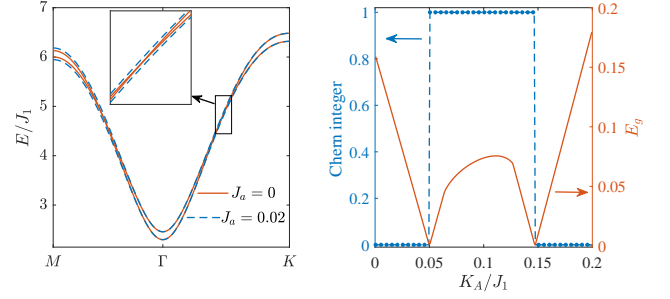


FIG. 2: (a) The magnon band structures at  $T = 0$  and  $K_A = 0.1$ . The other parameters are adopted as  $S = 2.5$ ,  $J_1 = 1.0$ ,  $I_1 = 0.05$ ,  $J_2^A = 0.08$ ,  $J_2^B = 0.065$ ,  $K_B = 0.05$ . All the parameters are in the unit  $J_1 = 1.54$  meV. In subsequent calculations, we adopt the same parameters when not pointing out in particular.  $J_a = 0$  for solid line and  $J_a = 0.02$  for dashed lines. (b) The Chern integer for the acoustic branch and bandgap with respect to  $K_A$  at  $T = 0$ . The other parameters are the same to (a) with  $J_a = 0.02$ . The bandgap is defined as  $E_g = \min_{\mathbf{k}} (E_{\mathbf{k}}^\beta - E_{\mathbf{k}}^\alpha)$  along  $\Gamma - \mathbf{K}$  direction.

vanishes at  $\Gamma$  and  $\mathbf{K}$  points, the band point touching at  $\Gamma$  ( $\mathbf{K}$ ) point when  $K_A = K_B$  ( $K_A = K_B + K_c$ ) will not be changed. Thus the two conditions give the phase boundaries between trivial and nontrivial topological phases. In Fig. 2 (a), we can see the two bands are gapped in the intersection region (dashed lines). Fig. 2 (b) gives the gap evolution along the  $\Gamma - \mathbf{K}$  direction. We use the Chern integer as the topological invariant, defined as  $C_\lambda = \frac{1}{2\pi} \int_{BZ} B_\lambda^z d^2\mathbf{k}$  with Berry curvature  $\mathbf{B}_\lambda = \nabla \times \mathbf{A}_\lambda$  and Berry connection  $\mathbf{A}_\lambda = i\text{Tr}[\Gamma^\lambda \Lambda_{\mathbf{k}}^\dagger \tau_z (\partial_{\mathbf{k}} \Lambda_{\mathbf{k}})]$ , where  $\Gamma^\lambda$  is the diagonal matrix taking +1 for  $\lambda$  mode and zero otherwise. We find the Chern integer is 1 inside the interval  $K_B < K_A < K_B + K_c$  for the acoustic branch, as presented in Fig. 2 (b). When the sublattice asymmetric second neighbor exchange interaction is reversed, i.e.,  $J_2^A < J_2^B$ , the nontrivial topological phase lies in the interval  $0 < K_B - K_A < K'_c$  and the Chern integer for the acoustic branch is -1 with  $K'_c \simeq 9(J_2^B - J_2^A)\bar{S}'/(4\bar{S} - 2S - 1)$ . In the subsequent discussions, we will focus on  $J_2^A > J_2^B$  as the two cases share the same physics.

We now consider the effect of nonlinear self-energy corrections at finite temperatures and show that the trivial bands at  $T = 0$  will also exhibit Chern insulating phase above a critical temperature before the paramagnetic phase transitions. We first present the phase diagram directly and choose the Chern integer of the acoustic branch as the order parameter, calculated from the effective Hamiltonian after the self-consistent treatment at given temperatures. The self-consistent process also helps us to confirm that the temperatures we choose are all below Néel temperature  $T_N$ . The phase diagram in the  $K_A - T$  plane is shown in Fig. 3 (a). We can see when  $K_B < K_A < K_B + K_c$ , the topological phase will not be destroyed by the nonlinear corrections, same to the previous works. Interestingly, when  $K_A < K_B$  and

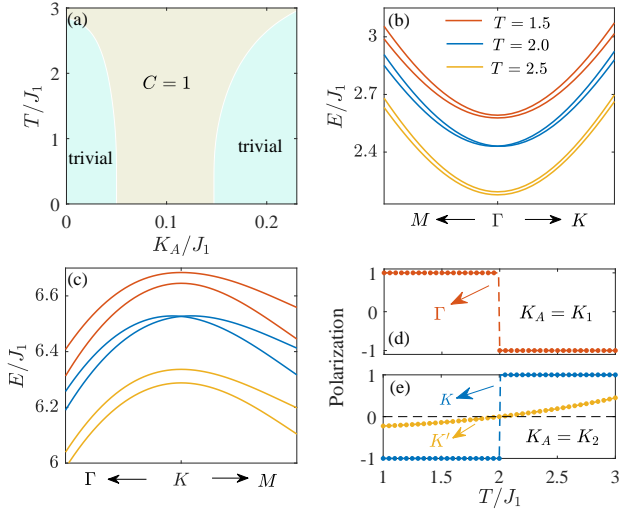


FIG. 3: (a) The phase diagram in the  $K_A - T$  plane. The Chern number is for the acoustic branch, while the Chern number for optical branch is opposite. The temperature unit is  $T_0 = J_1/k_B \simeq 17.9$  K with  $J_1 = 1.54$  meV. (b) Magnon bands near  $\Gamma$  point at three temperatures.  $K_A = K_1 = 0.041$ . (c) Magnon bands near  $K$  point at the same three temperatures to (b).  $K_A = K_2 = 0.169$ . At  $K_1$  and  $K_2$ , the critical temperature of topological transition is almost the same,  $T_c/J_1 \simeq 2$ . (d) The magnon chirality switch at  $\Gamma$  point for  $K_A = K_1$ . (e) The magnon chirality switch at  $K$  point and DoP evolution at  $K'$  point for  $K_A = K_2$ . For all the figures,  $J_a = 0.02$ .

$K_A > K_B + K_c$ , the magnon bands show trivial phase at low temperatures but exhibit Chern insulating phase above a critical temperature  $T_c$ , which is dependent on  $K_A$ . Note that here  $T_c$  is below the Néel temperature  $T_N$ . This phenomenon is quite surprising and is not presented or discussed in all the previous works on topological phase of magnons. This indicates that the thermal fluctuation can indeed induce a magnonic topological insulating phase when taking the nonlinear effect from MMIs into consideration. Note that the phase diagram is similar to the one of topological Anderson insulators,<sup>48-51</sup> where the thermal fluctuation strength (temperature) in our system is analog to the disorder strength.

To further investigate these thermal fluctuation induced topological transitions at finite temperature, we plot the magnon bands at three temperatures for  $K_A \simeq 0.041(K_1) < K_B$  and  $K_A \simeq 0.169(K_2) > K_B + K_c$  in Fig. 3 (b) and (c), respectively. The critical temperature of topological transition for the two values are almost the same,  $T_c/J_1 \simeq 2$ . For  $K_a = K_1$ , we plot the bands near  $\Gamma$  point. Besides the magnon energy renormalization, we can see the bandgap at  $\Gamma$  point decreases as the temperature increases. The spectrum become gapless at  $T = T_c$ . Further increasing temperature reopens the gap. During this process, we have checked the two bands at other points in the BZ are always gapped. From the phase diagram in Fig. 3 (a), the Chern number is 0

below  $T_c$  and 1 above  $T_c$ . The other  $K_A < K_B$  value shares the same behavior with different critical temperature  $T_c$ . Such temperature induced topological phase at the region  $K_A < K_B$  is related to the weak ferrimagnetic phase induced at finite temperatures (see Appendix B), which arises from the imbalanced occupation number of the two magnon branches. The zero bandgap condition at  $\Gamma$  point is  $K_A(-2S - 1 + 4\bar{S}_A) + 3(J_1 + I_1)\bar{S}_B = K_B(-2S - 1 + 4\bar{S}_B) + 3(J_1 + I_1)\bar{S}_A$ .  $\bar{S}_A \neq \bar{S}_B$  at finite temperature requires  $K_A < K_B$  for the topological transition in this case. Such temperature induced topological transition is totally due to the thermal fluctuation. That is to say, when  $K_a = K_b$ , a weak perpendicular magnetic field can replace the role of easy-axis asymmetry to get same results with a negative magnetic field. The phase diagram is presented in Appendix C. For  $K_A = K_2$ , the magnon bands experience a similar behavior but the gap closes and reopens at  $K$  point instead, as shown in Fig. 3 (c). For both cases, the thermal fluctuation induces gap closing and reopening and the topological invariant, i.e. Chern integer jumps from 0 to 1.

## B. Magnon chirality switch

The Néel vectors of two magnon modes precess circularly with opposite chiralities when  $J_a = 0$ .<sup>52</sup> For finite  $J_a$ , the precession trajectories will become elliptical. The polarization of the magnons in antiferromagnet is similar to the one of light. We can define the degree of polarization (DoP) for magnons in the momentum space. At a given  $\mathbf{k}$ , the eigenvector at finite  $J_a$  can be expressed as a linear combination of the polarized state at  $J_a = 0$ , so we have  $\Lambda_{\mathbf{k}}^\lambda = \chi_{\mathbf{k},\lambda}^+ \Lambda_{\mathbf{k}}^+ + \chi_{\mathbf{k},\lambda}^- \Lambda_{\mathbf{k}}^-$  ( $\lambda = \alpha, \beta$ ), where  $\Lambda_{\mathbf{k}}^\pm$  is the eigenvectors for right- and left-handed precession modes when  $J_a = 0$ ,  $\chi_{\mathbf{k},\lambda}^\pm$  the expansion coefficients and satisfying  $|\chi_{\mathbf{k},\lambda}^+|^2 + |\chi_{\mathbf{k},\lambda}^-|^2 = 1$ . The DoP in momentum space is defined as  $\mathcal{P}(\mathbf{k}) = |\chi_{\mathbf{k},\lambda}^+|^2 - |\chi_{\mathbf{k},\lambda}^-|^2$ . Below we will only focus on the acoustic branch, while the DoP for the optical branch is opposite. At zero temperature and  $J_a = 0$ , the chirality is right-handed for  $K_A < K_B$  ( $\mathcal{P}(\mathbf{k}) = 1$ ) and left-handed for  $K_A > K_B + K_c$  ( $\mathcal{P}(\mathbf{k}) = -1$ ). Finite  $J_a$  does not break the chirality at  $K$  and  $\Gamma$  points. Therefore, the chirality at  $K$  and  $\Gamma$

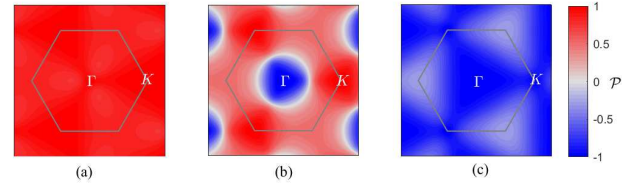


FIG. 4: The DoP distribution in the BZ in the three regions of phase diagram Fig. 3 (a) for the acoustic branch. We adopt  $K_A = 0.02$  in (a), 0.1 in (b) and 0.18 in (c). The temperature is set  $T = 1.5$ .



points in the left trivial region in the phase diagram of Fig. 3 (a) is right-handed, while at the right trivial region it is left-handed. In the middle topologically nontrivial region, we find the the chirality is right-handed at  $\mathbf{K}$  point, while left-handed at  $\Gamma$  point. These features indicate that the topological transitions are accompanied by a magnon chirality switch at where the gap closes and reopens. When  $K_A < K_B$ , the chirality will be switched from the right-handed to left-handed across  $T_c$ , as shown in Fig. 3 (d). On the other side  $K_A > K_B + K_c$ , the chirality will be switched from the left-handed to right-handed, as shown in Fig. 3 (e). Near the  $\mathbf{K}'$  point, the magnon will also experience chirality switch, same to  $\mathbf{K}$  point when  $J_a = 0$  and  $K_A > K_B + K_c$ . For finite  $J_a$ , the evolution of the DoP at  $\mathbf{K}'$  shows a negative to positive transition [see Fig. 3 (e)]. As reported in the experimental works,<sup>53–57</sup> the magnon polarization in antiferromagnets can be detected by the magneto-Raman spectroscopy,<sup>53</sup> the polarized neutron scattering technique<sup>54</sup> or polarization-selective spectroscopy.<sup>55–57</sup> These experimental methods greatly coincide with our system. The detection of the magnon polarization provide experimental proofs of the temperature induced topological transitions.

We briefly discuss the DoP in the full BZ. There are three different regions in the phase diagram in Fig. 3 (a). The typical DoP distributions in the BZ for the three regions are shown in Fig. 4 (a) (b) (c), respectively. In the left region, the DoP is positive [Fig. 4 (a)] and the right-handed mode dominates. While in the right region, the DoP is negative [Fig. 4 (c)] and the left-handed mode dominates. In the middle topological region,  $\mathcal{P}$  is negative near  $\Gamma$  point and positive around  $\mathbf{K}$  point [Fig. 4 (b)]. The ring-like transition zone where  $\mathcal{P} \simeq 0$  is the band intersection region when  $J_a = 0$ . The differences indicate that the temperature would change the distribution, the detection of which using the experimental techniques above provides alternative experimental proofs of our theory.

### C. Thermal Hall effect

The topological transitions from trivial to nontrivial phases indicate nontrivial transitions of the Berry curvature distribution in the momentum space. Therefore the topological transitions of magnons are expected to manifest themselves in the thermal transport properties.<sup>58,59</sup> The thermal Hall conductivity is given by

$$\kappa_{xy} = -\frac{k_B^2 T}{\hbar} \sum_{\lambda=\alpha,\beta} \int [d\mathbf{k}] B_{\lambda}^z(\mathbf{k}) c_2(n_{\mathbf{k},\lambda}). \quad (6)$$

where  $[d\mathbf{k}] = d^2\mathbf{k}/(2\pi)^2$ ,  $k_B$  is the Boltzmann constant,  $\hbar$  is the reduced Planck constant,  $c_2(x) = (1+x)(\log \frac{1+x}{x})^2 - (\log x)^2 - 2Li_2(-x)$ , and  $Li_2(x)$  is the polylogarithm function. We plot the temperature-dependent thermal Hall conductivities  $\kappa_{xy}$  in Fig 5 (a) and (b) with

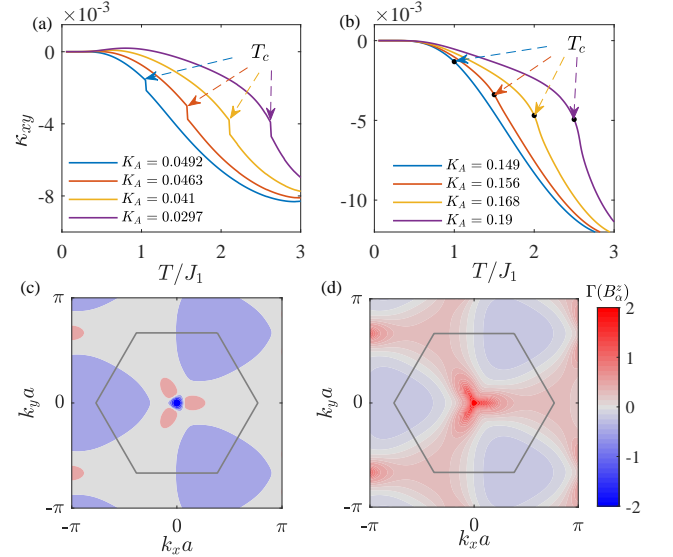


FIG. 5: (a) (b) The thermal Hall conductivity of four different  $K_A$  values for  $K_A < K_B$  and  $K_A > K_B + K_c$ , respectively. The corresponding critical temperature  $T_c$  is  $T_c/J_1 = 1, 1.5, 2, 2.5$ , respectively.  $\kappa_{xy}$  is in the unit  $k_B J_1 / \hbar = 3.23 \times 10^{-11}$  W/K for  $J_1 = 1.54$  meV. (c) (d) The distribution of Berry curvatures in log scale  $\Gamma(B_{\alpha}^z) = \text{sgn}(B_{\alpha}^z) \log_{10}(1 + |B_{\alpha}^z|)$  for (c)  $T/J_1 = 1.8$  and (d)  $T/J_1 = 2.2$  at  $K_A = 0.041$ . (c) (d) share the same colorbar. The gray hexagon denote the first Brillouin zone.

different  $K_A$  for comparison. We also give the Berry curvature distribution for a typical  $K_A$  value at the temperature below and above  $T_c$ , respectively.

For  $K_A < K_B$ , we give the  $\kappa_{xy}$  with four different values, corresponding to different  $T_c$ . We can see all the  $\kappa_{xy}$  show discontinuous behavior across  $T_c$ . This can be interpreted from the Berry curvature transition near the  $\Gamma$  point, as shown in Fig. 5 (c) and (d). The gap closes and reopens at  $\Gamma$  point and the Berry curvature experiences a jump from negative to positive values near  $\Gamma$  point. The discontinuity of  $\kappa_{xy}$  with respect to temperature is prominent and experimentally distinguishable. Therefore the thermal Hall effect of magnons provides another route to probe the topological transition experimentally.

For  $K_A > K_B + K_c$ , we can see  $\kappa_{xy}$  with respect to the temperature do not show a discontinuity near  $T_c$  [Fig. 5 (b)] This is because the thermal Hall effect of magnons are mainly contributed from the magnons with low energies. the bandgap closes and reopen at  $\mathbf{K}$  points with the energies quite large compared to  $k_B T_c$ . The nontrivial Berry curvature transition near  $\mathbf{K}$  point has negligible effect on  $\kappa_{xy}$ . As the case  $K_A < K_B$  is mostly experimentally approachable, thus the thermal Hall effect can be the indicator of the topological transitions of magnons in realistic experiments.

## D. Discussions

Above all, by challenging the belief in former works that thermal fluctuation can not induce a topological phase for magnons, we successfully build a Chern insulating phase above finite temperatures before the paramagnetic phase transition while the magnon bands at zero temperature is topologically trivial. The system is the collinear antiferromagnetic insulator MnPS<sub>3</sub> with sublattice asymmetries induced in homobilayer or heterostructures. We also propose realistic schemes to detect these transitions experimentally. As the bond dependent term is equivalent to the nearest neighbor dipolar interactions, which exist generally between the local spins in magnets. Recent neutron resonance spin echo spectroscopy verified the band splitting due to the dipolar interactions in MnPS<sub>3</sub>.<sup>41,60</sup> Therefore, our proposal and results should be universal in all the two-dimensional collinear antiferromagnets with sublattice asymmetries and not limited to the honeycomb lattices. Another van der Waals magnet MnPSe<sub>3</sub><sup>61,62</sup> is also promising candidate material. Since our proposal is based on the broken of sublattice symmetry, the ferrimagnets,<sup>63</sup> lacking it naturally, are expected to exhibit similar temperature-induced topological phase transitions.

## IV. SUMMARY

In summary, we demonstrate that thermal fluctuation in magnets can induce nontrivial topological phase for magnons at finite temperature while at low temperature the bands are trivial. The transition between trivial and nontrivial topological phases can be probed with multiple state-of-the-art techniques via measuring the thermal Hall conductivity or detecting the magnon polarization. The temperature dependent topological phase is quite important for designing topological devices at easily achievable higher temperatures. Our work paves the way for the study of the interplay between topological orders, MMIs and thermal fluctuation that is beyond the linear spin wave theory.

## V. ACKNOWLEDGMENTS

Y.-M. Li thanks Dr. Ya-Jie Wu and Dr. Bin Wei for helpful discussions. This work is supported by the startup funding from Xiamen University.

### Appendix A: the expressions for the self-energies

We here use the Green function method and random phase approximation to get the nonlinear self-energy corrections. The Heisenberg equation-of-motion for the

Green function is given by

$$\begin{aligned}\frac{d\hat{G}(\mathbf{k}, \tau)}{d\tau} &= -\delta(\tau)\tau_z - \langle T[H, \Psi_{\mathbf{k}}(\tau)]\Psi_{\mathbf{k}}^\dagger(0) \rangle \\ &= -\delta(\tau)\tau_z - \tau_z(H_{\mathbf{k}} + \Sigma_{\mathbf{k}})\hat{G}(\mathbf{k}, \tau).\end{aligned}$$

Here the self-energy term  $\Sigma_{\mathbf{k}}$  is from the random phase approximation. With the Fourier transformation  $\hat{G}(\mathbf{k}, \tau) = (1/\beta)\sum_n \hat{G}(\mathbf{k}, \omega_n)e^{-i\omega_n\tau}$ , we can get  $-i\omega_n\hat{G}(\mathbf{k}, \omega_n) = -\tau_z - \tau_z(H_{\mathbf{k}} + \Sigma_{\mathbf{k}})\hat{G}(\mathbf{k}, \omega_n)$ . Thus

$$[i\omega_n - \tau_z(H_{\mathbf{k}} + \Sigma_{\mathbf{k}})]\hat{G}(\mathbf{k}, \omega_n) = \tau_z.$$

By multiply a  $\tau_z$  term on the both side, we can get the Dyson's equation in the main text.

From the diagonalization matrix  $\Lambda_{\mathbf{k}}$ , we have the relation  $a_{\mathbf{k}} = u_{\mathbf{k},a,\alpha}\alpha_{\mathbf{k}} + u_{\mathbf{k},a,\beta}\beta_{\mathbf{k}} + v_{-\mathbf{k},a,\alpha}\alpha_{-\mathbf{k}}^\dagger + v_{-\mathbf{k},a,\beta}\beta_{-\mathbf{k}}^\dagger$ , also  $b_{\mathbf{k}} = u_{\mathbf{k},b,\alpha}\alpha_{\mathbf{k}} + u_{\mathbf{k},b,\beta}\beta_{\mathbf{k}} + v_{-\mathbf{k},b,\alpha}\alpha_{-\mathbf{k}}^\dagger + v_{-\mathbf{k},b,\beta}\beta_{-\mathbf{k}}^\dagger$ . We here calculate the simplest term  $\Sigma_{\mathbf{k}}^{12}$  to show how to get the relation in Eq. (5). As  $\Sigma_{\mathbf{k}}^{12} = -\frac{J_a g_{\mathbf{k}}}{2} \frac{1}{N} \sum_{\mathbf{q}} (\langle a_{\mathbf{q}}^\dagger a_{\mathbf{q}} \rangle + \langle b_{\mathbf{q}}^\dagger b_{\mathbf{q}} \rangle)$ . Using the relation above, we have

$$\begin{aligned}\sum_{\mathbf{q}} \langle a_{\mathbf{q}}^\dagger a_{\mathbf{q}} \rangle &= \frac{1}{N} \sum_{\mathbf{q}} (|u_{\mathbf{q},a,\alpha}|^2 \langle \alpha_{\mathbf{q}}^\dagger \alpha_{\mathbf{q}} \rangle + |u_{\mathbf{q},a,\beta}|^2 \langle \beta_{\mathbf{q}}^\dagger \beta_{\mathbf{q}} \rangle \\ &\quad + |v_{-\mathbf{q},a,\alpha}|^2 \langle \alpha_{-\mathbf{q}} \alpha_{-\mathbf{q}}^\dagger \rangle + |v_{-\mathbf{q},a,\beta}|^2 \langle \beta_{-\mathbf{q}} \beta_{-\mathbf{q}}^\dagger \rangle) \\ &= \sum_{\mathbf{q}} [|u_{\mathbf{q},a,\alpha}|^2 n_{\mathbf{q},\alpha} + |u_{\mathbf{q},a,\beta}|^2 n_{\mathbf{q},\beta} \\ &\quad + |v_{-\mathbf{q},a,\alpha}|^2 (1 + n_{-\mathbf{q},\alpha}) + |v_{-\mathbf{q},a,\beta}|^2 (1 + n_{-\mathbf{q},\beta})] \\ &= \sum_{\mathbf{q}, \lambda=\alpha, \beta} (|u_{\mathbf{q},a,\lambda}|^2 + |v_{\mathbf{q},a,\lambda}|^2) n_{\mathbf{q},\lambda} + |v_{\mathbf{q},a,\lambda}|^2,\end{aligned}$$

and

$$\sum_{\mathbf{q}} \langle b_{\mathbf{q}}^\dagger b_{\mathbf{q}} \rangle = \sum_{\mathbf{q}, \lambda=\alpha, \beta} (|u_{\mathbf{q},b,\lambda}|^2 + |v_{\mathbf{q},b,\lambda}|^2) n_{\mathbf{q},\lambda} + |v_{\mathbf{q},b,\lambda}|^2.$$

So we have

$$\begin{aligned}\Sigma_{\mathbf{k}}^{12} &= -\frac{1}{N} \sum_{\mathbf{q}, \lambda=\alpha, \beta} \sum_{\xi=a, b} \frac{J_a g_{\mathbf{k}}}{2} [|u_{\mathbf{q},\xi,\lambda}|^2 + |v_{\mathbf{q},\xi,\lambda}|^2] n_{\mathbf{q},\lambda} \\ &\quad + |v_{\mathbf{q},\xi,\lambda}|^2\end{aligned}$$

Comparing to Eq. (5), we can set  $T_{12}^\lambda(\mathbf{k}, \mathbf{q}) = -\frac{J_a g_{\mathbf{k}}}{2} \sum_{\xi=a, b} (|u_{\mathbf{q},\xi,\lambda}|^2 + |v_{\mathbf{q},\xi,\lambda}|^2)$  and  $Q_{12}^\lambda(\mathbf{k}, \mathbf{q}) = -\frac{J_a g_{\mathbf{k}}}{2} \sum_{\xi=a, b} |v_{\mathbf{q},\xi,\lambda}|^2$ . The other elements of the self-energy can also obtained with the same method above, then we can get the expressions in Eq. (5) in the main text.

### Appendix B: temperature-induced weak ferrimagnetic phase

Due to sublattice asymmetries, the band degeneracies is broken. At finite temperatures, the occupation number for the two bands is different  $n_{\mathbf{q},\alpha} > n_{\mathbf{q},\beta}$ . This will

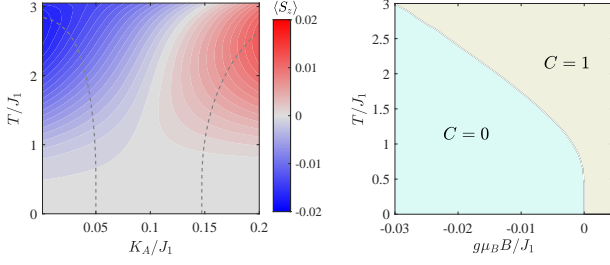


FIG. 6: (a). The total magnetization  $\langle S_z \rangle$  distribution in the  $K_A$ - $T$  plane. The dashed gray lines are the phase boundaries adopted from Fig. 3 (a). (b). Phase diagram under magnetic field.  $K_A = K_B = 0.05$ . The other parameters are the same to the main text.

induce a weak ferrimagnetic phase. The total magnetization along  $z$  direction is defined as  $\langle S_z \rangle = \bar{S}_A - \bar{S}_B = \frac{1}{N} \sum_{\mathbf{k}} \langle b_{\mathbf{k}}^\dagger b_{\mathbf{k}} \rangle - \langle a_{\mathbf{k}}^\dagger a_{\mathbf{k}} \rangle$ . From Fig 6 (a), we can see  $\langle S_z \rangle$  does not equal to zero at relatively high temperatures. The two band touching at  $\Gamma$  point should satisfy the condition  $K_A(-2S - 1 + 4\bar{S}_A) + 3(J_1 + I_1)\bar{S}_B =$

$K_B(-2S - 1 + 4\bar{S}_B) + 3(J_1 + I_1)\bar{S}_A$ . When  $K_A = K_B$  and neglecting the MMIs,  $\langle S_z \rangle = 0$ , the two magnon bands are always degenerate at  $\Gamma$  point although  $J_2^A \neq J_2^B$ . But at finite temperature,  $\langle S_z \rangle \neq 0$ , zero band gap condition at  $\Gamma$  point satisfies for certain value of  $K_A$  with  $K_A < K_B$ , giving rise to the topological transitions at finite temperatures in the main text.

### Appendix C: phase diagram under a weak magnetic field

A weak perpendicular magnetic field can replace the role of easy-axis anisotropy asymmetry according to the above analysis for the band gap closing condition at  $\Gamma$  point in the BZ. We set  $K_A = K_B$  to verify this. The phase diagram is shown in Fig. 6 (b). At zero temperature, a positive magnetic field gives a nontrivial topological phase for magnetic field, while a negative one gives a trivial phase. Across a magnetic field dependent critical temperature, the trivial phase can also go into nontrivial phase.

\* Corresponding author: [yunmeili@xmu.edu.cn](mailto:yunmeili@xmu.edu.cn)

- <sup>1</sup> M. Z. Hasan, and C. L. Kane, Colloquium: Topological insulators, *Rev. Mod. Phys.* **82**, 3045 (2010).
- <sup>2</sup> X.-L. Qi and S.-C. Zhang, Topological insulators and superconductors, *Rev. Mod. Phys.* **83**, 1057 (2011).
- <sup>3</sup> N. P. Armitage, E. J. Mele, and A. Vishwanath, Weyl and Dirac semimetals in three-dimensional solids, *Rev. Mod. Phys.* **90**, 015001 (2018).
- <sup>4</sup> B. A. Bernevig, T. L. Hughes, and S.-C. Zhang, Quantum Spin Hall Effect and Topological Phase Transition in HgTe Quantum Wells, *Science* **314**, 1757 (2006).
- <sup>5</sup> M. S. Miao, Q. Yan, C. G. Van de Walle, W.-K. Lou, L. L. Li, and Kai Chang, Polarization-Driven Topological Insulator Transition in a GaN/InN/GaN Quantum Well, *Phys. Rev. Lett.* **109**, 186803 (2012).
- <sup>6</sup> D. Zhang, W. K. Lou, M. S. Miao, S. C. Zhang, and Kai Chang, Interface-Induced Topological Insulator Transition in GaAs/Ge/GaAs Quantum Wells, *Phys. Rev. Lett.* **111**, 156402 (2013).
- <sup>7</sup> S.-Y. Xu, Y. Xia, L. A. Wray, S. Jia, F. Meier, J. H. Dil, J. Osterwalder, B. Slomski, A. Bansil, H. Lin, R. J. Cava, and M. Z. Hasan, Topological Phase Transition and Texture Inversion in a Tunable Topological Insulator, *Science* **332**, 560 (2011).
- <sup>8</sup> P. Dziawa, B. J. Kowalski, K. Dybko, R. Buczko, A. Szczerbakow, M. Szot, E. Łusakowska, T. Balasubramanian, B. M. Wojek, M. H. Berntsen, O. Tjernberg, and T. Story, Topological crystalline insulator states in  $\text{Pb}_{1-x}\text{Sn}_x\text{Se}$ , *Nat. Mater.* **11**, 1023 (2012).
- <sup>9</sup> F. Zhao, T. Cao, and S. G. Louie, Topological Phases in Graphene Nanoribbons Tuned by Electric Fields, *Phys. Rev. Lett.* **127**, 166401 (2021).
- <sup>10</sup> I. Garate, Phonon-Induced Topological Transitions and Crossovers in Dirac Materials, *Phys. Rev. Lett.* **110**, 046402 (2013).
- <sup>11</sup> B. M. Wojek, M. H. Berntsen, V. Jonsson, A. Szczerbakow, P. Dziawa, B. J. Kowalski, T. Story, and O. Tjernberg, Direct observation and temperature control of the surface Dirac gap in a topological crystalline insulator, *Nat Commun* **6**, 8463 (2015).
- <sup>12</sup> G. Antonius, and S. G. Louie, Temperature-Induced Topological Phase Transitions: Promoted versus Suppressed Nontrivial Topology, *Phys. Rev. Lett.* **117**, 246401 (2016).
- <sup>13</sup> T. Imai, J. Chen, K. Kato, K. Kuroda, T. Matsuda, A. Kimura, K. Miyamoto, S. V. Ereemeev, and T. Okuda, Experimental verification of a temperature-induced topological phase transition in  $\text{TlBiS}_2$  and  $\text{TlBiSe}_2$ , *Phys. Rev. B* **102**, 125151 (2020).
- <sup>14</sup> P. Aguado-Puente and P. Chudzinski, Thermal topological phase transition in  $\text{SnTe}$  from ab initio calculations, *Phys. Rev. B* **106**, L081103 (2022).
- <sup>15</sup> L. Lu, J. D. Joannopoulos, and Marin Soljačić, Topological photonics, *Nature Photon.* **8**, 821 (2014).
- <sup>16</sup> J. Lu, C. Qiu, L. Ye, X. Fan, M. Ke, F. Zhang, and Z. Liu, Observation of topological valley transport of sound in sonic crystals, *Nature Phys.* **13**, 369 (2017).
- <sup>17</sup> R. Shindou, R. Matsumoto, S. Murakami, and J.-ichiro Ohe, Topological chiral magnonic edge mode in a magnonic crystal, *Phys. Rev. B* **87**, 174427 (2013).
- <sup>18</sup> Y.-M. Li, J. Xiao, and K. Chang, Topological magnon modes in patterned ferrimagnetic insulator thin films, *Nano Lett.* **18**, 3032 (2018).
- <sup>19</sup> Z. Hu, L. Fu, and L. Liu, Tunable Magnonic Chern Bands and Chiral Spin Currents in Magnetic Multilayers, *Phys. Rev. Lett.* **128**, 217201 (2022).
- <sup>20</sup> L. Zhang, J. Ren, J.-S. Wang, and B. Li, Topological magnon insulator in insulating ferromagnet, *Phys. Rev. B* **87**, 144101 (2013).
- <sup>21</sup> A. Mook, J. Henk, and I. Mertig, Edge states in topological

- magnon insulators, *Phys. Rev. B* **90**, 024412 (2014).
- 22 R. Chisnell, J. S. Helton, D. E. Freedman, D. K. Singh, R. I. Bewley, D. G. Nocera, and Y. S. Lee Topological Magnon Bands in a Kagome Lattice Ferromagnet, *Phys. Rev. Lett.* **115**, 147201 (2015).
  - 23 S. K. Kim, H. Ochoa, R. Zarzuela, and Y. Tserkovnyak, Realization of the Haldane-Kane-Mele Model in a System of Localized Spins, *Phys. Rev. Lett.* **117**, 227201 (2016).
  - 24 T. Hirose, S. A. Díaz, J. Klinovaja, and D. Loss, Magnonic Quadrupole Topological Insulator in Antiskyrmion Crystals, *Phys. Rev. Lett.* **125**, 207204 (2020).
  - 25 H. Kondo and Y. Akagi, Dirac Surface States in Magnonic Analogs of Topological Crystalline Insulators, *Phys. Rev. Lett.* **127**, 177201 (2021).
  - 26 X. S. Wang, H. W. Zhang, and X. R. Wang, Topological Magnonics: A Paradigm for Spin-Wave Manipulation and Device Design, *Phys. Rev. Applied* **9**, 024029 (2018).
  - 27 Y.-M. Li, Y.-J. Wu, X.-W. Luo, Y. Huang, and K. Chang, Higher-order topological phases of magnons protected by magnetic crystalline symmetries, *Phys. Rev. B* **106**, 054403 (2022).
  - 28 Y.-S. Lu, J.-L. Li, and C.-T. Wu, Topological Phase Transitions of Dirac Magnons in Honeycomb Ferromagnets, *Phys. Rev. Lett.* **127**, 217202 (2021).
  - 29 A. Mook, K. Plekhanov, J. Klinovaja, and D. Loss, Interaction-Stabilized Topological Magnon Insulator in Ferromagnets, *Phys. Rev. X* **11**, 021061 (2021).
  - 30 A. V. Chumak, V. I. Vasyuchka, A. A. Serga, and B. Hillebrands, Magnon spintronics, *Nature Phys.* **11**, 453 (2015).
  - 31 V. Baltz, A. Manchon, M. Tsoi, T. Moriyama, T. Ono, and Y. Tserkovnyak, Antiferromagnetic spintronics, *Rev. Mod. Phys.* **90**, 015005 (2018).
  - 32 F. J. Dyson, General Theory of Spin-Wave Interactions, *Phys. Rev.* **102**, 1217 (1956).
  - 33 T. Oguchi, Theory of Spin-Wave Interactions in Ferro- and Antiferromagnetism, *Phys. Rev.* **117**, 117 (1960).
  - 34 S. H. Liu, Nonlinear Spin-Wave Theory for Antiferromagnets, *Phys. Rev.* **142**, 267 (1966).
  - 35 B.-G. Liu, A non-linear spin-wave theory of quasi-2D quantum Heisenberg antiferromagnets, *J. Phys.: Condens. Matter* **4**, 8339 (1992).
  - 36 S. S. Pershoguba, S. Banerjee, J. C. Lashley, J. Park, H. Ågren, G. Aeppli, and A. V. Balatsky, Dirac Magnons in Honeycomb Ferromagnets, *Phys. Rev. X* **8**, 011010 (2018).
  - 37 Z. Li, T. Cao, S. G. Louie, Two-dimensional ferromagnetism in few-layer van der Waals crystals: Renormalized spin-wave theory and calculations, *J. Magn. Magn. Mater.* **463**, 28 (2018).
  - 38 B. Wei, J.-J. Zhu, Y. Song, K. Chang, Renormalization of gapped magnon excitation in monolayer  $\text{MnBi}_2\text{Te}_4$  by magnon-magnon interaction, *Phys. Rev. B* **104**, 174436 (2021).
  - 39 V. V. Mkhitarian and L. Ke, Self-consistently renormalized spin-wave theory of layered ferromagnets on the honeycomb lattice, *Phys. Rev. B* **104**, 064435 (2021).
  - 40 T. Matsumoto, and S. Hayami, Nonreciprocal magnons due to symmetric anisotropic exchange interaction in honeycomb antiferromagnets, *Phys. Rev. B* **101**, 224419 (2020).
  - 41 T. J. Hicks, T. Keller, A. R. Wildes, Magnetic dipole splitting of magnon bands in a two dimensional antiferromagnet, *J. Magn. Magn. Mater.* **474**, 512 (2019).
  - 42 R. Hidalgo-Sacoto, R. I. Gonzalez, E. E. Vogel, S. Allende, J. D. Mella, C. Cardenas, R. E. Troncoso, and F. Munoz, Magnon valley Hall effect in  $\text{CrI}_3$ -based van der Waals heterostructures, *Phys. Rev. B* **101**, 205425 (2020).
  - 43 F. Xiao and Q. Tong, Tunable Strong Magnetic Anisotropy in Two-Dimensional van der Waals Antiferromagnets, *Nano Lett.* **22**, 3946 (2022).
  - 44 A. Mook, S. A. Díaz, J. Klinovaja, and D. Loss, Chiral hinge magnons in second-order topological magnon insulators, *Phys. Rev. B* **104**, 024406 (2021).
  - 45 J. B. Fouet, P. Sindzingre, and C. Lhuillier, An investigation of the quantum  $J_1 - J_2 - J_3$  model on the honeycomb lattice, *Eur. Phys. J. B* **20**, 241 (2001).
  - 46 K. H. Lee, S. B. Chung, K. Park, and J.-G. Park, Magnonic quantum spin Hall state in the zigzag and stripe phases of the antiferromagnetic honeycomb lattice, *Phys. Rev. B* **97**, 180401(R) (2018).
  - 47 A. L. Fetter, and J. D. Walecka, Quantum Theory of Many-Particle Systems (Dover Books on Physics), McGraw-Hill, New York, 2003.
  - 48 J. Li, R.-L. Chu, J. K. Jain, and S.-Q. Shen, Topological Anderson Insulator, *Phys. Rev. Lett.* **102**, 136806 (2009).
  - 49 S. Stützer, Y. Plotnik, Y. Lumer, P. Titum, N. H. Lindner, M. Segev, M. C. Rechtsman, and A. Szameit, Photonic topological Anderson insulators, *Nature* **560**, 461 (2018).
  - 50 E. J. Meier, F. A. An, A. Dauphin, M. Maffei, P. Massignan, T. L. Hughes, B. Gadway, Observation of the topological Anderson insulator in disordered atomic wires, *Science* **362**, 929 (2018).
  - 51 X.-W. Luo, C. Zhang, Non-Hermitian Disorder-induced Topological insulators, *arXiv.1912.10652*.
  - 52 S. M. Rezende, A. Azevedo, and R. L. Rodríguez-Suárez, Introduction to antiferromagnetic magnons, *J. Appl. Phys.* **126**, 151101 (2019).
  - 53 J. Cenker, B. Huang, N. Suri, P. Thijssen, A. Miller, T. Song, T. Taniguchi, K. Watanabe, M. A. McGuire, D. Xiao, and X. Xu, Direct observation of two-dimensional magnons in atomically thin  $\text{CrI}_3$ , *Nat. Phys.* **17**, 20 (2021).
  - 54 Y. Nambu, J. Barker, Y. Okino, T. Kikkawa, Y. Shiomi, M. Enderle, T. Weber, B. Winn, M. Graves-Brook, J. M. Tranquada, T. Ziman, M. Fujita, G. E. W. Bauer, E. Saitoh, and K. Kakurai, Observation of Magnon Polarization, *Phys. Rev. Lett.* **125**, 027201 (2020).
  - 55 Y. Liu, Z. Xu, L. Liu, K. Zhang, Y. Meng, Y. Sun, P. Gao, H.-W. Zhao, Q. Niu, and J. Li, Switching magnon chirality in artificial ferrimagnet, *Nat. Commun* **13**, 1264 (2022).
  - 56 Y. Shiota, T. Arakawa, R. Hisatomi, T. Moriyama, and T. Ono, Polarization-Selective Excitation of Antiferromagnetic Resonance in Perpendicularly Magnetized Synthetic Antiferromagnets, *Phys. Rev. Applied* **18**, 014032 (2022).
  - 57 T. Arakawa, Y. Shiota, K. Yamada, T. Ono, and S. Kon, Magnetic polarization selective spectroscopy of magnetic thin films probed by wide-band crossed microstrip circuit in GHz regime, *Review of Scientific Instruments* **93**, 013901 (2022).
  - 58 H. Katsura, N. Nagaosa, P. A. Lee, Theory of the Thermal Hall Effect in Quantum Magnets, *Phys. Rev. Lett.* **104**, 104, 066403 (2010).
  - 59 R. Matsumoto, S. Murakami, Theoretical Prediction of a Rotating Magnon Wave Packet in Ferromagnets, *Phys. Rev. Lett.* **106**, 197202 (2011).
  - 60 A. R. Wildes, B. Roessli, B. Lebech, and K W Godfrey, Spin waves and the critical behaviour of the magnetization in  $\text{MnPS}_3$ , *J. Phys.: Condens. Matter* **10**, 6417 (1998).



- <sup>61</sup> B. L. Chittari, Y. Park, D. Lee, M. Han, A. H. MacDonald, E. Hwang, and J. Jung, Electronic and magnetic properties of single-layer  $\text{MPX}_3$  metal phosphorous trichalcogenides, [Phys. Rev. B \*\*94\*\*, 184428 \(2016\)](#).
- <sup>62</sup> S. Calder, A. V. Haglund, A. I. Kolesnikov, and D. Mandrus, Magnetic exchange interactions in the van der Waals layered antiferromagnet  $\text{MnPSe}_3$ , [Phys. Rev. B \*\*103\*\*, 024414 \(2021\)](#).
- <sup>63</sup> M. Mi, X. Zheng, S. Wang, Y. Zhou, L. Yu, H. Xiao, H. Song, B. Shen, F. Li, L. Bai, Y. Chen, S. Wang, X. Liu, Y. Wang, Variation between Antiferromagnetism and Ferrimagnetism in  $\text{NiPS}_3$  by Electron Doping, [Adv. Funct. Mater. \*\*32\*\*, 2112750 \(2022\)](#).